# Convolutional Neural Network (CNN) Based Martian Dune Detection

Nayama Valsa Scariah<sup>1\*</sup>, Mili Ghosh Nee Lala<sup>1</sup>, Akhouri Pramod Krishna<sup>1</sup> Birla Institute of Technology, Mesra, Ranchi, India<sup>1</sup> E-mail: nayama99@gmail.com, mili@bitmesra.ac.in, apkrishna@bitmesra.ac.in \*Corresponding author

Keywords: aeolian, Martian dune, CNN, U-Net, ResUNet, ResUNet++

Received: October 10, 2024

Sand dunes are one of the most prominent Aeolian landforms present on the Martian surface. Accumulation and erosion of sand particles cause the formation of dunes, which possibly can influence the Martian climate too. For mapping such landforms over large areas of the Martian surface more effectively, automated detection of dunes has been brought out. For this a convolutional neural network (CNN) based detection approach has been implemented considering application of different models and assessing their respective performance using different sets of Orbiter images. CNN architectures such as U-net, ResUNet and ResUNet++ were used for segmentation of dunes over the Martian surface. CNN produced segmentation results with greater accuracy with advantage of designing new models and using different loss functions. Convolution neural networks such as U-Net, ResUNet, and ResUNet++ for detecting dunes on Martian surface used Context camera (CTX) and the High-Resolution Imaging Experiment (HiRISE) images of Mars Reconnaissance Orbiter (MRO) to generate the suitable models considering two different Martian sites, Gale crater and Nili Patera. The models thus generated were tested over Olympia Undae region of the Mars and all the architectures could produce more than 85% accuracy. The model created using CTX images performed well for Gale Crater region compared to the model created using HiRISE image. U-Net model created using CTX image performed well in case of low-quality images (coarse resolution noisy images) whereas, ResUNet ++ model created using HiRISE image performed well in case of good quality (fine resolution) images.

Povzetek: Za kartiranje sipin na Marsu iz orbiterjevih posnetkov so uporabili CNN segmentacijo (U-Net, ResUNet, ResUNet++) na CTX in HiRISE (učenje: Gale, Nili Patera; test: Olympia Undae). Rezultati: vse >85 %; U-Net+CTX za slabše slike, ResUNet++ + HiRISE za visokoločljive.

#### 1 Introduction

Sand dunes are the most prominent aeolian landforms on the Martian surface and considered crucial agents of climate, wind regime, sediment type, and transportation on mars (Urso et al., 2018). On the Martian surface, the dunes were first observed by Mariner-9 (Sagan and Bagnold 1975). Martian surface has the aeolian activity predominantly in the absence of liquid water and active volcanism or tectonic deformation (Greeley et al., 2000). Wind can transport and deposit sand particles from one place to another and such wind process leads to modification of existing land forms as well as creation of new landforms such as sand dunes. Changes in wind direction led to the formation of different types of sand dunes. They are classified into barchan dunes, barchanoid ridge, transverse dunes, linear dunes, star dunes, and reversing dunes (Mckee, 1979). Mapping of these features would provide an idea about the current and past climate and weather systems.

Wind fluxes alter the morphology of dune fields from barchans to barchanoids and longitudinal dunes to isolated domes and ending up with sand sheets (Runyon, 2016). Martian dune fields are mainly distributed in high latitudinal region and polar regions with their predominance in low plains and thereafter, craters, canyons as well as intermontane depressions (Chao and Zhibao, 2022). Mars Global Digital Dune database provides idea about the distribution of dunes on the Martian surface (Hayward, 2014). For automatic detection of such dunes, neural network based deep learning methods could be effective. Neural network designed to model in such a way that it performs a particular task similar to human brain. Human brain acts entirely in a different manner from the traditional digital computers since it is highly complex, nonlinear and behaves like a parallel computer. It acquires knowledge from environment through learning process and synaptic weights are used to save the knowledge (Hayden, 2009).

Automatic detection techniques can allow generation of landform maps over a large area in a short time. Many automated detection algorithms have been used to detect landforms on the Martian surface and other planetary surfaces. Most of the automatic detections have been carried out in impact craters on Mars compared to any other landforms (Martins et al., 2009, Bandeira et al.,

2007). There are some other methods used for detecting craters, such as template matching (Bandeira et al., 2007) and boosting approach (Martins et al., 2009). Different filters and decision trees have also been used for detecting craters (Stepinski and Tomasz, 2009). Automatic detection of sand dunes in Mars was carried out by using Histogram Oriented Gradient (HOG) for feature extraction; and Support Vector Machine (SVM) and Boosting techniques for classification (Bandeira et al., 2012). Convolutional neural networks (CNN) have become more popular in recent years. In Lunar surface, craters have been detected from DEM (Digital Elevation Models) using U-Net architecture (Silburt et al., 2019). Volcanic rootles cones (VTCs) and Transverse Aeolian Ridges (TAR) in Mars automatically detected by using a convolution neural network named MarsNet (Palafox et al., 2017). Automatic detection technique such as linear segment detection algorithm was used to determine dune orientation and sand supply on the surface of Titan (Lucas et al., 2014). It combined the dune migration with wind field generated by climatic models. Mask regional convolution neural network (Mask-RCNN) predicts the mask on each Region of Interest (RoI) along with classification and bounding box regression carried out in Faster-RCNN (He et al.,2016). Mask-RCNN is an extension of Faster RCNN. Mask-RCNN was used for the detection and segmentation of barchan dunes on Martian surface (Rubanenko et al., 2021). U-Net, ResUNet, and ResUNet++ required fewer training samples than Mask-RCNN, and it also excels in segmenting fine-grained details (Munawar, 2023).

In our study, we have considered convolution neural networks such as U-Net, ResUNet, and ResUNet++ for detecting dunes on Martian surface. Deep neural networks require large amount of annotated data for training, but U-Net outperforms such neural networks with limited amount of data. U-Net architecture consists mainly of a contracting path and expanding path (Ronneberger et al., 2015). U-Net has been useful in various remote sensing applications such as land cover classification (Ulmas and Liiv, 2020), segmentation of clouds (Sánchez-Bayton et al., 2022) and segmentation of buildings (Wagner et al., 2022). ResUNet integrates the residual neural network and U-Net architecture. It mainly consists of an encoder, decoder and a bridge connecting between them. It provides better performance with fewer parameters (Zhang et al., 2018). ResUNet++ architecture consists of residual blocks, squeeze and excitation block, Atrous Spatial Pyramid Pooling (ASPP) and attention block (Jha et al., 2019). It enhances for the purpose of performance trial of the automatic sand dune detection model, a test site named Olympia Undae region situated between 78°N to 83°N latitude and 120°E to 240°E longitude was selected. It is the largest dune field on the Martian surface (https://mars.nasa.gov/resources/26259/olympia-undae/). This site is situated in the Northern polar region of Mars whereas, Gale crater is situated in southern equatorial region and Nili Patera is situated in northern hemisphere close to the equator.

# 2 Materials and methods

HiRISE and CTX images were used towards automated sand dune detection model development. HiRISE image onboard Mars Reconnaissance Mission is a pushbroom imaging system with focal length of about 12m effective length and has 14 CCD detectors. It has spatial resolution of about 25-32 cm/pixel depending upon on the altitude of space craft and the off-nadir roll angle. It acquires data in three different channels, such as blue-green (~536nm), red (~692nm) and near-infrared (~874nm). Ten detectors are used for red filter and each two filters are used for bluegreen and near-infra red filters. The HiRISE RDR products are stored in JPEG2000 with 10-bit imaging system ranging from 0-1023 (Eliason E. et al., 2012). CTX is the one of the primary payloads of Mars Reconnaissance Orbiter. It uses catadioptric telescope with focal length of about 350mm. Kodak KLI-5001G detector with 5056pixel linear CCD detect a visible broad band of light from 500 to 700 nm. CCD used the push broom scanner along the direction of spacecraft motion. CTX has spatial resolution of about ~6m/pixel. It acquires monochromatic images of Martian surface (Wolff et al., 2013).

### 2.1. Study area

Two different regions on the Martian surface were considered for developing automatic detection models for sand dunes. Such study sites include Gale crater and Nili Patera regions. Gale crater is situated between latitude 2.25°S to 8.25°S and longitude 133.25°E to 140.25°E (Figure. 1a). It is an impact structure with a diameter of 154 km (Schwenzer et al., 2012). Gale is a crater probably a dry lake on Mars near the north-western part of the Aeolis quadrangle (Palucis et al., 2016). It is estimated to be about~3.6 billion years old (Wray, 2013). Aeolis mons is a mountain in the centre of Gale and rises 5.5km high above the crater floor. Curiosity rover landed on Gale crater for identifying the habitability of the Martian surface. The minerals present in the lower part of the sedimentary strata in the Mount Sharp within Gale crater indicate transition from warm to cold climate in the Martian atmosphere (Rampe et al., 2019).

Nili patera region extends from 8.46°N to 19.41°N latitude and 58.88°E to 76.644°E longitude (Figure. 1b). It is a 50 km diameter caldera at the centre of the Syrtis Major Planum. It contains different landforms and distinctive mineral deposits. Syrtis major planum is of Hesperian- age (Fawdon et al., 2015). Nili patera region has the most active dust storm season in the Martian surface. It is an old volcanic region with different interesting features. This region is a low relief area with slope of less than 1° (Mubarak et al., 2019, Hood et al., 2021).

For the purpose of performance trial of the automatic sand dune detection model, a test site named Olympia Undae region situated between 78°N to 83°N latitude and 120°E to 240°E longitude was selected. It is the largest dune field the Martian (https://mars.nasa.gov/resources/26259/olympia-undae/).

This site is situated in the Northern polar region of Mars whereas, Gale crater is situated in southern equatorial region and Nili Patera is situated in northern hemisphere close to the equator.

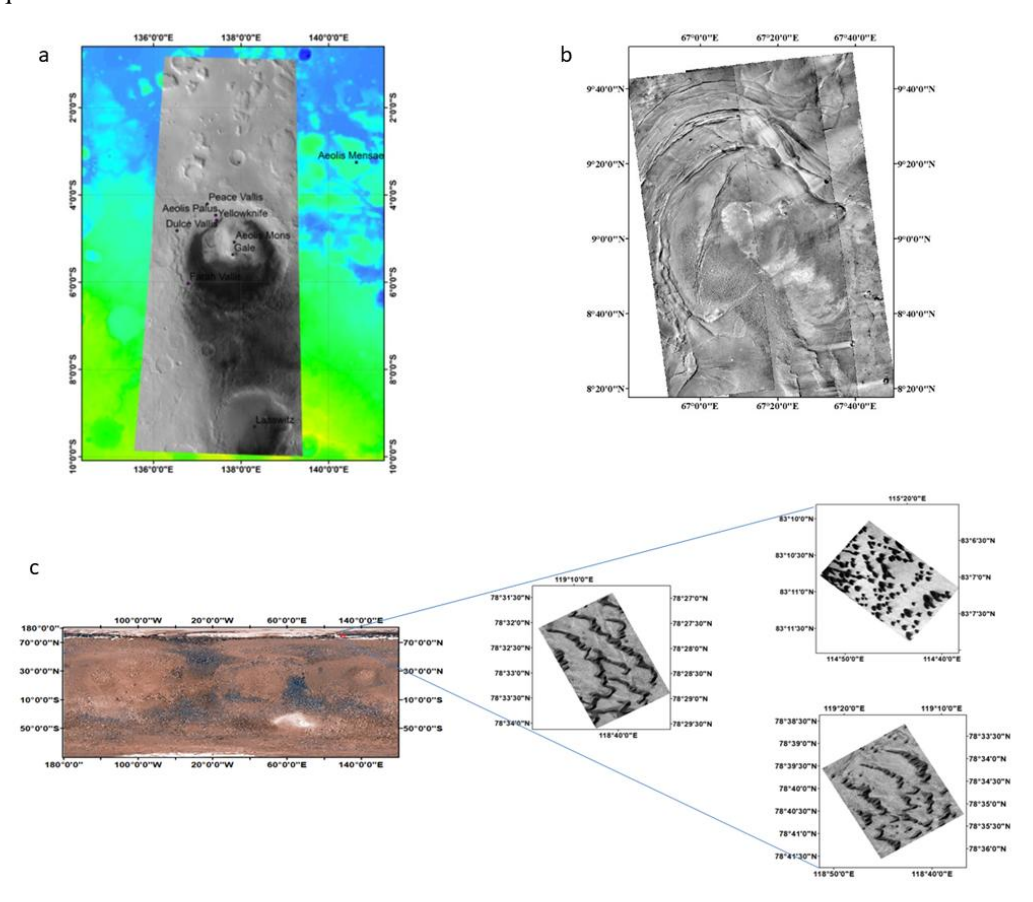


Figure 1a: HiRISE image of Gale crater b. CTX image of Nili Patera region c. Location selected from Olympia Undae region

## 2.2. Methodology

Datasets selected out of CTX and HiRISE images pertaining to Gale crater (4.07S to 6.66S latitude and 136.51E to 139.12E longitude) and Nili Patera (1.37S to 19.41N latitude and 58.88E to 76.644E longitude) regions respectively were further analyzed. AI-based approach has been considered for extraction of dunes. The architecture pertaining to convolution neural networks (CNN) such as U-Net, ResUNet, and ResUNet++ were implemented in Keras after (Vasilev et al., 2019) with tensorflow in python. The system configuration Windows 10 o/s with cuda version 10.0 and cuDNN version 7.6.5 was used. Data augmentation techniques such as rotation, horizontal flip, vertical flip, horizontal translation, vertical translation etc. were implemented. It led to increase in the training data sets thus generated with 7000 HiRISE and 7160 CTX dune images respectively. A batch size of 16 using Adam optimizer with loss function as dice, binary cross-entropy and mean squared error were used. From the augmented datasets, 80% were used for training, 10% for testing, and 10% for validation. Apart from using the training dataset used for training the model, validation datasets were used

to tune the hyper-parameters of the model. For this, the test data was used for the model accuracy assessment after the model had been fully trained (after Myrianthous 2021). In the convolution layer, a kernel was applied to the original image, convolution was performed to move the filter. For example, the filter moves two columns right and does convolution for a stride of two. If the input image is considered 7x7 matrix and the filter size 3x3 with a stride of two, then the output becomes 3x3 matrix. Upon completion of the convolution, maxpooling operation was performed. In this process, maximum value was picked from a 2x2 filter. There are also other pooling available such as average pooling and global pooling. To enhance the results, batch normalization was required for keeping the values in the input and hidden layers within a certain range and allowing improvement in the training speed. Thereafter, dropout step could be added for dropping out of neurons at random in the neural network to prevent over fitting. Further to this, flattening led the data to culminate in to the dense layer by converting the two-dimensional dataset into one-dimensional data or converting the data into a single column

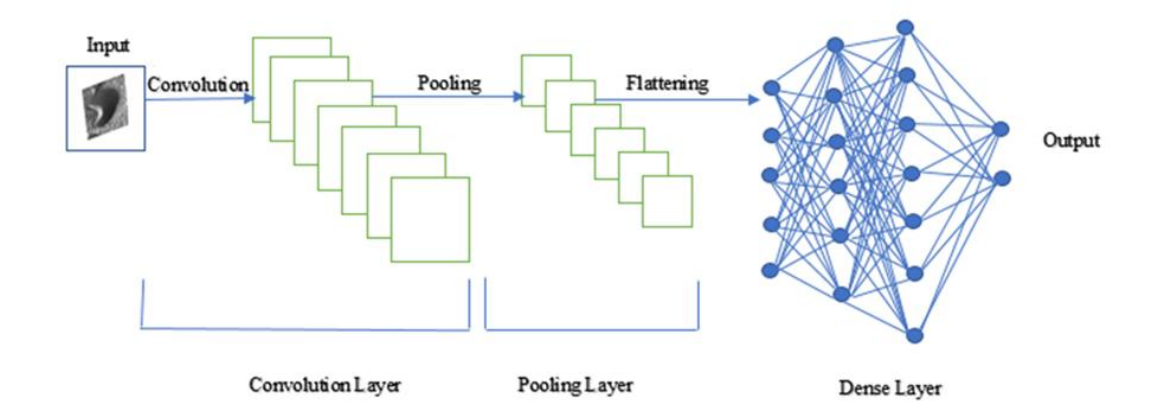


Figure 2: Architecture of convolutional neural network

The dense layer connects different neurons with each neuron associated with weight, bias, and activation function. If the weight is high, then the neuron is good, if the bias is above a certain threshold value, then the neuron is active, if the bias is below the threshold value, then the neuron is dead. The neurons go through the activation function which decides whether the neuron is active or not. Multiple convolution and pooling layers were added to the architecture.

Overall methodology that used for the study is given in figure 3. The dunes were identified from CTX and HiRISE images. Create binary images such as "1" indicate for dune and "0" for non-dune images in ImageJ platform. Create segmentation models by using UNet, ResUNet and ResUNet++ architectures for CTX and HiRISE images. After image segmentation compare the results obtained from different architectures and different images.

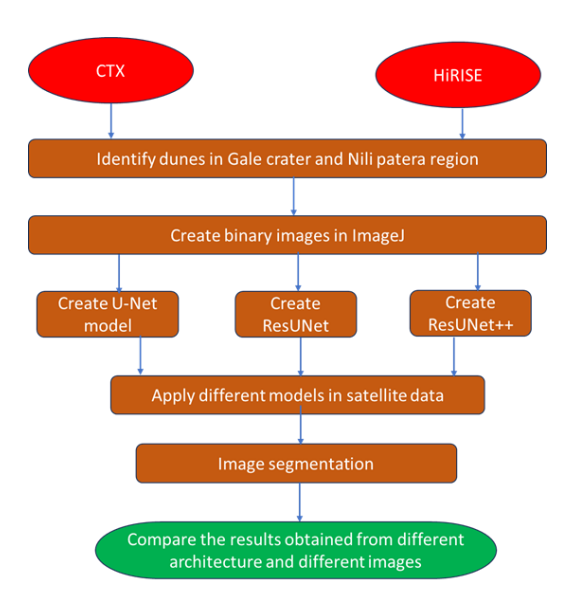


Figure 3. Overall workflow

#### 2.2.1 U-Net architecture

U-Net is a particular type of architecture used for image segmentation. In this architecture, deep learning tools are arranged in such a way that it can be used for image segmentation. It is called U-Net because it looks like "U" and it consists of an encoder and decoder path (figure 4). Concatenation of feature maps helps to give localization information (Ronneberger et al., 2015). The input image size was considered 128x128x3 and a color image with size 128x128 was fed into the input layer with a feature space of 16. Thus, the output of the convolution layer (C1) became 128x128x16. Thereafter, upon performing a

maxpooling operation with a stride of 2 gave rise to an output as 64x64x16 (P1); after doing two convolution operations with feature space of 32, output was obtained as 64x64x32 (C2) and the process continued till obtaining C5 (figure 4). Thereafter, up sampling was performed where 8x8x256 (C5) became 16x16x128 and concatenated it with C4, then the final value at U6 became16x16x256 (U6+C4). After a couple of convolution layers; the output became 16x16x128 (C6), and finally going through U7 to U9, the output would be 128x128x1.

#### 2.2.2. ResUNet architecture

ResUNet as the combination of both U-Net and residual neural network consists of one decoder path, one encoder path and a bridge connecting both encoder and decoder. The residual units consist of two 3x3 convolution block and an identity mapping. Each identity mapping connects the input and output of the residual block. Each convolutional block consists of one batch normalization, one Rectified Linear Unit (ReLU) activation layer, and one

convolutional layer (Figure 5).

In encoding units, a stride of two was applied instead of using pooling operation unlike U-Net architecture in order to reduce the size of the feature map. Before each decoding unit, there is an up sampling of feature maps from the lower level and concatenation with the feature maps from the corresponding encoding path. After the decoding path to obtain a segmented image, a 1x1 convolution with a sigmoid activation is applied (Zhang et al., 2018)

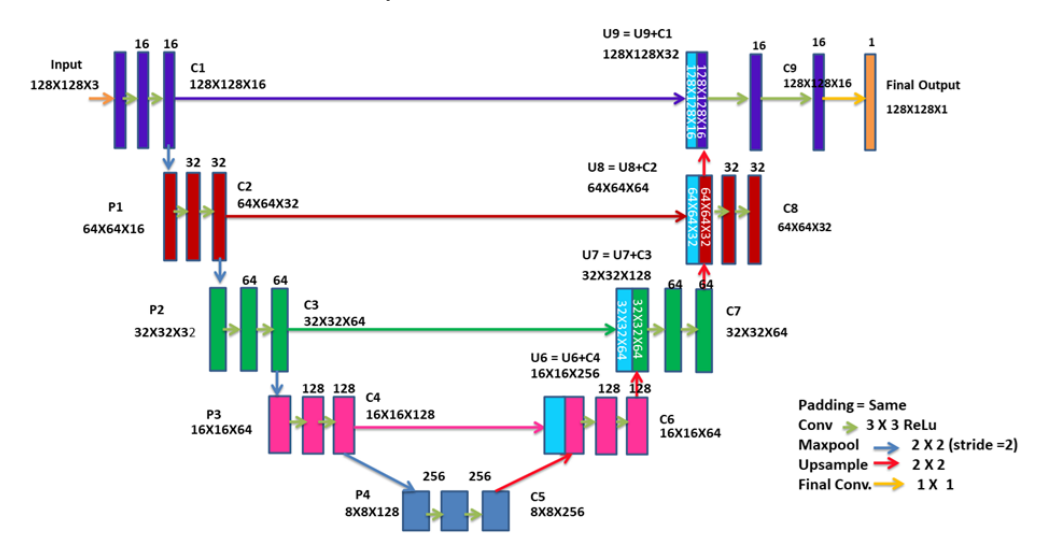


Figure 4: Architecture of U-Net (Ronneberger et al., 2015)

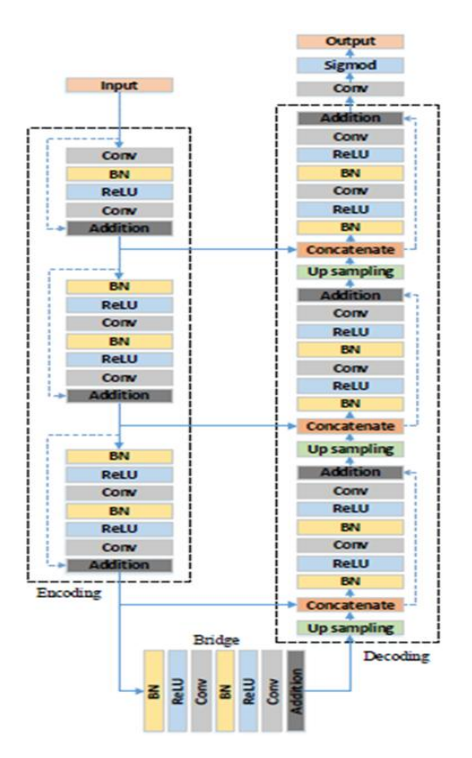


Figure 5: ResUNet architecture (Zhang et al., 2018)

#### 2.2.3 ResUNet++ Architecture

As a combination of both U-Net and residual neural networks (He et.al., 2016), the ResUNet++ (Figure 6) consists of one stem block, three encoder blocks, Astrous Pyramidal Pooling (ASPP), and three decoder blocks (Jha et al., 2019). The residual unit combines two 3x3 convolution layers, batch normalization, ReLU activation, and an Identity mapping. Each Identity mapping connects the input and output of the encoder block. The outcome of each encoder block passes through the squeeze and excitation block (Hu et al., 2018), which increases the interrelationship between the channels. The global average pooling was used in squeezing operation to extract a single value for each channel. The excitation produced a channelwise weight, with two fully connected layers; a ReLU activation function, and then a sigmoid activation function. Inside, the excitation operation, there are two fully connected layers with compression between the layers. Each weight signified dependencies between the channels, and it provided the degree of freedom to our network to learn which channel was essential and its reliance.

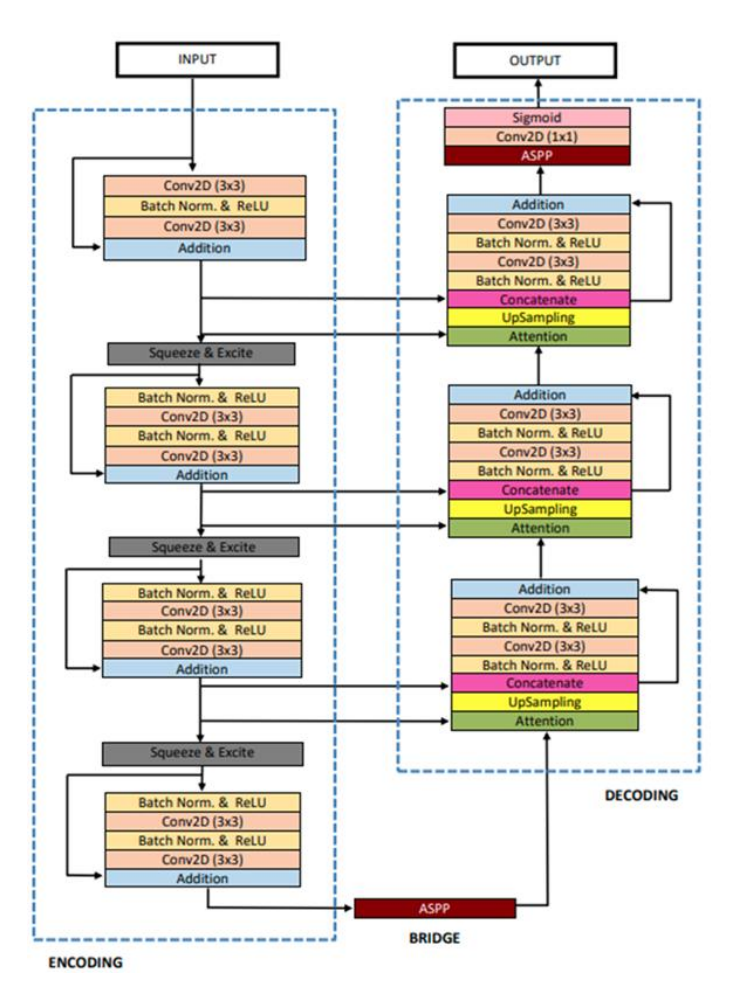


Figure 6: Architecture of ResUNet ++ (Jha et al., 2019)

ASPP acts as a bridge between encoder and decoder blocks with 3x3 convolution layers. Different rates are applied to the input feature maps and all these outputs fuse together. ASPP helps detect the object with different scales, improving accuracy (Chen et al., 2016). The output from the ASPP goes through attention unit which gives a subset of the input units by providing concentration to particular parts in the neural network (Vaswani et al., 2017). As inputs go through the dense layer and pass through the softmax layer, the outputs with different weights are obtained, followed by multiplication of these weights with the input vectors. Upon providing these outputs to another dense layer and the sigmoid activation function, segmented images are obtained.

Upon comparing the segmentation results of dunes obtained from U-Net, ResUNet and ResUNet++ by using HRSC and CTX images, different loss functions were applied. The best loss functions were chosen for each

architecture and hyperparameter optimization was done to obtain the best results. All these models were applied and tested in Olympia Undae region in the north polar region of the Mars.

#### 3 Results and discussion

#### 3.1 Dune segmentation using CTX images

For training the data,7160 training data were used which contained some noise data too. After applying different architectures such as U-Net, ResUNet and ResUNet++ for the segmentation of dunes, different loss functions and different hyper parameters such as number of epochs, learning rate, optimizer, batch size etc. were considered for selecting the best.

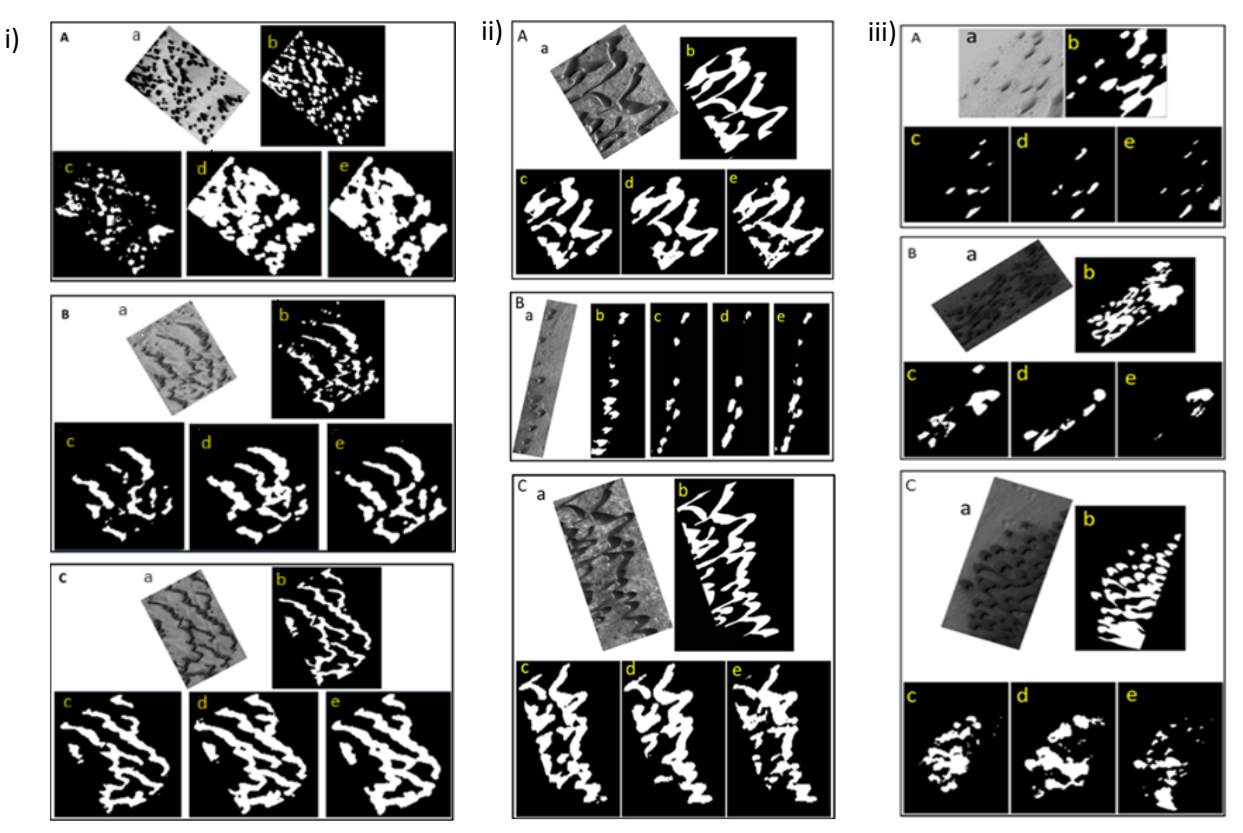


Figure 7: Dune field in i) Olympia Undae, ii) Nili Patera and iii) Gale Crater at three location A, B and C. Figure a. gray scale image b. ground truth image c. U-Net segmented image d. ResUNet segmented image e. ResUNet++ segmented image for model developed by CTX image

Mean squared error was used as loss function for ResUNet and ResUNet++ whereas, binary cross entropy loss was used for U-Net architecture. Segmented results were obtained from the three models developed using CTX image and the ground truth images. Results of segmentation are shown in Figure 7 for Olympia Undae, Nili Patera and Gale Crater respectively.

The models developed using CTX and HiRISE images were applied over Olympia Undae which is a dune field in the north polar region (Sánchez-Bayton, 2022), Gale Crater and Nili Patera. Confusion matrix elements such as TN (True Negative), TP (True Positive), FN (False Negative) and FP(False Positive) were obtained from manually digitized binary image as ground truth and the model predicted images.

Figure 7 explains the dune field in three locations in Olimpia Undae, Nili Patera and Gale Crater region. In each image, a and b show the grayscale image and ground truth image, as well as c, d, and e, shows the segmented images of UNet, ResUNet and ResUNet++ architecture, respectively. In Olimpia Undae, the segmented results of UNet more resembles to the ground truth image. The ResUNet and ResUNet++ show false positive results, such as some of the no-dune regions classified as dunes. In Nili Patera region segmented results of UNet and ResUNet++ produce similar results with ground truth images. However, the ResUNet shows false negative results, such

as some of the dune areas being misclassified as no-dune areas. In the Gale Crater region, all three architectures classified the dune pixel as a no-dune pixel.

Accuracy assessment after dune segmentation was arrived at through confusion matrix involving inferences on accuracy parameters such as Jaccard index, Precision, Recall, F1 scores and Accuracy. Jaccard index, also known as the Intersection over union (IoU), is a standard index for the segmentation results. It is the ratio of the Intersection of pixels between predicted image and mask image to the total number of pixels. The precision is the number of selected items that are relevant, and it is the ratio of the true positive to the sum of true positive and true negative. Recall is the number of relevant items that are selected, and it is the ratio of the true positive to the sum of true positive and false negative. F1 score is also known as the dice loss, which is the harmonic mean of precision and recall. Accuracy is the ratio of correctly classified pixel to the total number of pixels (Borg et al., 2020).

#### **Error** estimation of segmented images

Probability of error was also used for examining the performance of the model using following equations:

Probability of False negative:  $\rho_{FN} = \frac{FN}{(FN+TP)}$ Probability of False positive:  $\rho_{FP} = \frac{FN}{(FP+TN)}$ Global error:  $\rho_{error} = \rho_N \times \rho_{FP} + \rho_P \times \rho_{FN}$  Here FN represents the false negative pixel which signifies classification of dune pixels as non-dunes, FP is the false positive pixel which signifies classification of non-dune pixels as dunes, TP represents the true positive pixel which signifies classification of dune pixels as dune and TN represents true negative pixels, where non-dune pixels are classified as non- dune.  $\rho_N$  and  $\rho_P$  are probability of occurrence of negative and positive cells (Bandiera et al., 2012).

U-Net gave the best precision and accuracy compared to ResUNet and ResUNet++ architecture in case of Olympia Undae and Nili Patera regions (Table 1). ResUNet++ has the highest Recall, F1 score and Jaccard for these two regions as compared to Gale crater.

Table 1: Accuracy and error evaluated for the dune segmentation models created using CTX image	Ta	ble	: 1: 7	Accuracy	v and	l error eva	luated	for	the	dune	segmentati	on mod	lels	created	using	CTX	imag	es
--	----	-----	--------	----------	-------	-------------	--------	-----	-----	------	------------	--------	------	---------	-------	-----	------	----

Study	Method	Precision	Recall	F1-	Jaccard	Accuracy	$ ho_{ ext{FN}}$	$ ho_{ ext{FP}}$	$ ho_{ m error}$
region				score					
Olipmia	U-Net	0.80	0.62	0.68	0.52	0.93	0.38	0.03	0.22
Undae	ResUNet	0.56	0.93	0.68	0.52	0.88	0.08	0.13	0.17
	ResUNet++	0.58	0.95	0.71	0.56	0.89	0.05	0.12	0.14
Gale	U-Net	0.79	0.27	0.37	0.24	0.84	0.73	0.02	0.20
Crater	ResUNet	0.69	0.21	0.29	0.17	0.82	0.79	0.03	0.19
	ResUNet++	0.85	0.19	0.30	0.18	0.84	0.81	0.01	0.16
Nili	U-Net	0.85	0.75	0.78	0.65	0.95	0.25	0.03	0.18
Patera	ResUNet	0.69	0.86	0.76	0.62	0.93	0.14	0.08	0.17
	ResUNet++	0.69	0.88	0.77	0.63	0.93	0.13	0.07	0.16

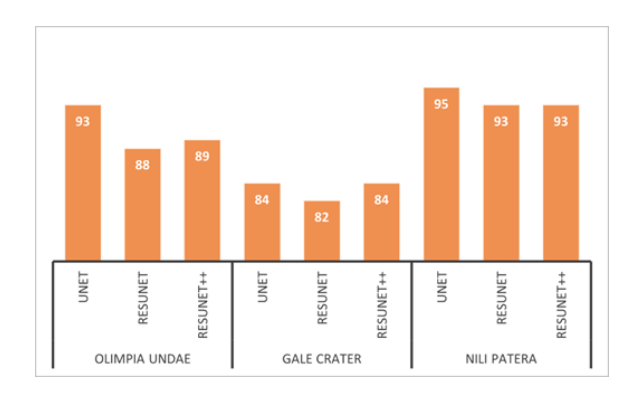


Figure 8: Accuracy assessment of results obtained from UNet, ResUNet and ResUNet++ models developed from CTX image in Olimpia Undae, Gale crater and Nili Patera region

ResUNet++ showed low error varying from 14.2% to 16.1% for all the regions compared to U-Net and ResUNet. U-Net showed the highest false negative error and lowest false positive error, whereas ResUNet++ showed the lowest false negative error and ResUNet had the largest false positive error for Olympia Undae and Nili Patera regions (Table 1.)

It was observed that (figure 8) UNet shows highest accuracy as compared to ResUNet and ResUNet++ in Olimpia Undae and Nili Patera region. ResUNet shows lowest accuracy in all the study area except Nili Patera region. From

the accuracy assessment, it is clear that the performance of the model affects the surface properties of the location as well.

# 3.2 Dune segmentation using HiRISE images

For training the model, 7000 HIRISE images were used. Dice was opted as the best loss function for ResUNet architecture, whereas mean squared error was used for U-Net and ResUNet++. The results obtained from these models are shown in figure 9 for Olympia Undae, Gale Crater and Nili Patera.

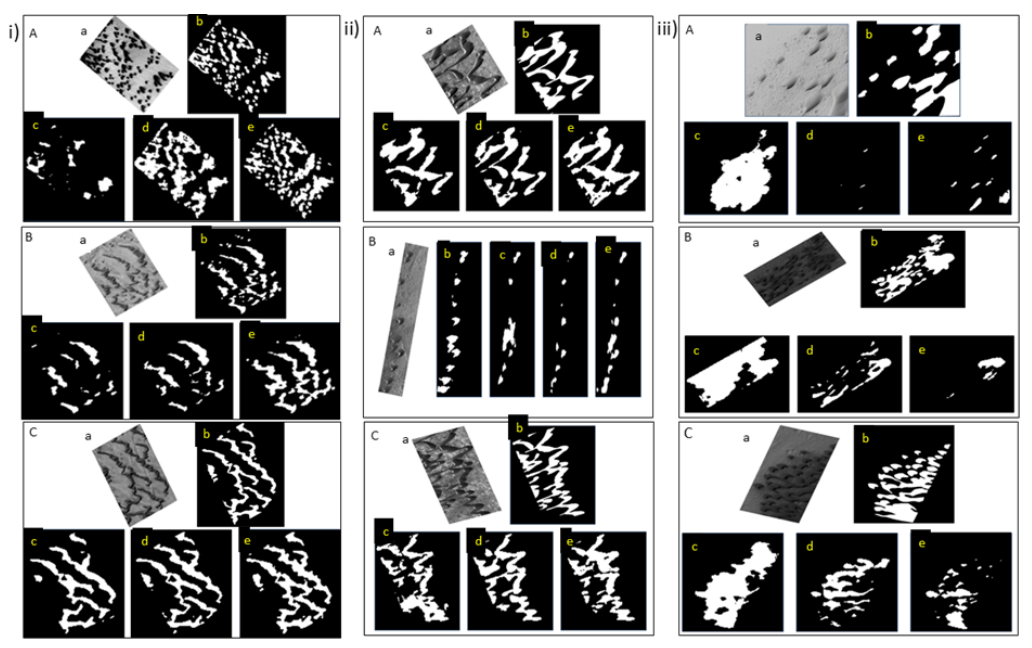


Figure 9: Segmentation results on i) Olympia Undae ii) Nili Patera and iii) Gale crater at three location A, B and C. Figure a. gray scale image b. ground truth image c. U-Net segmented image d. ResUNet segmented image e. ResUNet++ segmented image for model developed by HiRISE image

TE 11 0 A	1	C		1	•	II.DICE .
Table 2: Accuracy	AVAIHATION	tor seamen	tation of	diinec	າາເາກຕ	HIRINE IMAGE
rabic 2. Accuracy	Cvanuanon	TOI SUBINCI	itation or	uuncs	usmg	THINIDL IIIIage

				T		1	1	1	T
Study region	Method	Precision	Recall	F1-	Jaccard	Accuracy	$ ho_{ ext{FN}}$	$ ho_{ ext{FP}}$	$ ho_{ m error}$
				score					
OlympiaUndae	U-Net	0.84	0.53	0.62	0.47	0.92	0.47	0.02	0.22
	ResUNet	0.79	0.80	0.77	0.63	0.94	0.20	0.04	0.17
	ResUNet++	0.71	0.87	0.78	0.64	0.93	0.13	0.06	0.17
Gale crater	U-Net	0.46	0.70	0.55	0.39	0.79	0.30	0.19	0.33
	ResUNet	0.86	0.27	0.36	0.24	0.85	0.73	0.02	0.18
	ResUNet++	0.90	0.20	0.31	0.19	0.84	0.80	0.01	0.16
Nili Patera	U-Net	0.74	0.69	0.71	0.57	0.93	0.31	0.04	0.22
	ResUNet	0.89	0.66	0.73	0.60	0.95	0.34	0.02	0.18
	ResUNet++	0.80	0.77	0.78	0.65	0.95	0.23	0.03	0.19

Figure 9 explains the dune field in three locations in Olimpia Undae, Nili Patera and Gale Crater region. In each image, a and b show the grayscale image and ground truth image, as well as c, d, and e, shows the segmented images of UNet, ResUNet and ResUNet++ architecture, respectively. ResUNet++ produce better segmentation results in all three locations in Olimpia Undae region whereas, UNet classifies dune pixels as no-dune pixels in this region. In the Nili Patera region, ResUNet segmentation results resemble the ground truth image, whereas UNet and ResUNet++ models classify no-dunes as dunes. In Gale Crater region, the dunes were not properly segmented. UNet classified some of the no-dune pixels as dunes as well as ResUNet and ResUNet++ classified some of the dune pixels as no-dune pixels.

ResUNet and ResUNet++ architecture showed the highest accuracy for all the regions. ResUNet++ exhibited the highest recall, F1-score and Jaccard compared to U-Net and ResUNet architecture for Olympia Undae and Nili Patera regions (Table 2).

ResUNet++ shows low error of about 16.6% and 15.5 % for Olympia Undae and Gale crater regions as compared to other models (Table 2.). U-Net showed the highest error for all three regions.

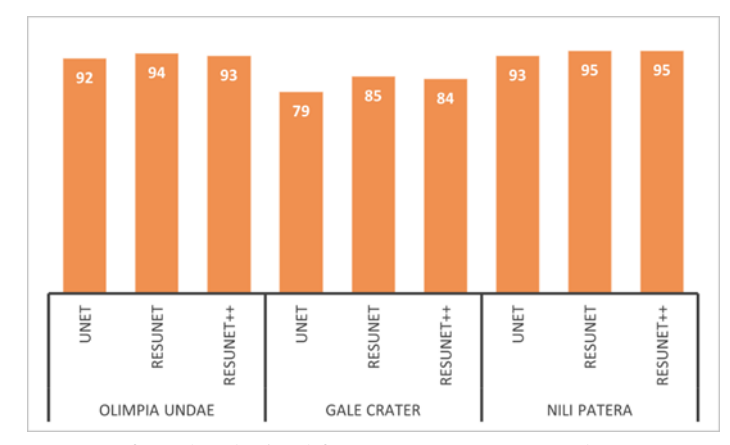


Figure 10: Accuracy assessment of results obtained from UNet, ResUNet and ResUNet++ models developed from HiRISE image in Olimpia Undae, Gale crater and Nili Patera region

It was observed that (figure 10) ResUNet shows the highest accuracy as compared to UNet and ResUNet++ in the Olimpia Undae and Nili Patera region. UNet shows the lowest accuracy in all the study areas except the Nili Patera region. All the architectures produce satisfactory results except UNet in Gale Crater, as it is one of the most windactive regions on Mars.

#### 3.3 Synthesis of dune segmentation achieved

For dune detection using AI, the data were trained in NVIDIA GeForce 940MX GPUs. To avoid overfitting, early stopping was used in the keras callbacks. In the early stopping process, the training process was stopped when the validation dataset started to decay, which meant validation loss started to increase or accuracy decreased. Most of the models reached a plateau at nearly the 10<sup>th</sup>epoch.

The best results were saved for each epoch and Adam optimizer was used for all the architectures. This is one of such studies, probably the first, for dune segmentation over the Martian surface using U-Net, ResUNet and ResUNet++ utilizing CTX and HiRISE data.

From the analysis it was clear that ResUNet++ had the high Recall/completeness in Olympia Undae and Nili Patera regions for model created by both HiRISE and CTX images as compared to U-Net and ResUNet models. Completeness of the model is denoted by Recall which is a measure of correctly classified positive samples by the model. Recall doesn't consider the negative samples classified as positive. Precision denotes the true detection among all the detection. U-Net showed the lowest false

positive rate for both CTX and HiRISE based segmentation for all the study regions. U-Net exhibited high F1-score and Jaccard index for the segmentation model created using CTX image for Gale crater and Nili Patera regions, whereas ResUNet++ had high F1-score and Jaccard index for the segmentation model created using HiRISE image for Olympia Undae and Nili Patera regions. Jaccard index and F1 score was helpful in assessing quality of the model. ResUNet++ model produced the best quality dune segmented image for model created using HiRISE image for Olympia Undae and Nili Patera regions. UNet produced high quality segmented images for model created using CTX image for Gale Crater and Nili Patera regions. As a whole, U-Net produced the better segmentation results from model created using CTX images. Whereas in case of models created using HiRISE images, ResUNet++ produced better results.

Accuracy obtained from U-Net, ResUNet and ResUNet++ models derived both from CTX and HiRISE image was high (more than 85%) for Olympia Undae and Nili Patera as compared to the results obtained from deep learning (82.01%) by (Azzaoui, et al., 2019).

Even minor features were delineated using ResUNet++ model developed using HiRISE images but in other models, the minor features turned out to be grouped. Some small dune features were not detected in U-Net architecture whereas, such features were detected in ResUNet and ResUNet++. The U-Net model could segment the linear dune features more accurately compared to small barchans and barchanoid dunes. ResUNet and ResUNet++ models could segment all the features with high accuracy.

# 3.4 Comparison of proposed and existing methods

Table 3: Comparison of proposed and existing methods with suitable
metrics

Matrics	UNet, ResUNet, ResUNet++	Other architecture
Dice coefficient	Higher value	Segnet, FCN have lower accuracy but DeepLabv3+ and PSPNet have
		higher accuracy
IoU	ResUNet++ has higher IoU value	DeepLabv3+ performs better than
	followed by ResUNet and UNet	U-Net and ResUNet
Precision	ResUnet++ has higher precision	DeepLabv3+ and PSPNet have
		same precision as ResUNet
Recall	Higher recall value	SegNet and FCN have lower recall
		value as well as SegNet and FCN
		have same recall value as ResUnet
F1 Score	ResUNet++ has higher F1 score	SegNet and FCN have lower F1
	value followed by ResUNet and	score value.
	UNet	

The comparison of proposed segmentation architectures, such as UNet, ResUNet, and ResUNet++, with existing architectures like SegNet, FCN, DeepLabv3+, and PSPNet has been shown in Table 3. The results obtained from different architectures (UNet, ResUNet, and ResUNet++) that were used in this study were compared with the results obtained from other existing architectures (Zhao P. et.al., 2025, Lu A. et.al., 2024, Gupta D., 2023). UNet, ResUNet and ResUNet++ shows better results as compared to other models. DeepLabv3+ and PSP Net show significantly reliable results.

#### 4 Conclusion

Different convolutional neural network architectures such as U-Net, ResUNet and ResUNet++ were used for the segmentation of dunes over the Martian surface. Different batch sizes, optimizers and loss functions were analyzed to select the best combination. A batch size of sixteen, Adam optimizer, and loss functions such as binary cross-entropy, dice loss and mean squared error were used.

After analyzing all the architectures, it was found that these architectures could produce satisfactory results of about 80% accuracy. The model created using CTX images performed well for Gale Crater region compared to the model created using HiRISE image. U-Net model created using CTX image performed well in case of low-quality images (coarse resolution noisy images) whereas, ResUNet ++ model created using HiRISE image performed well in case of good quality (fine resolution) images. The model created using CTX image showed low probability of error compared to the model created using HiRISE image. Therefore, model complexity and overfitting are related to each other. If the model is very complex, it affects the overfitting of the model. Due to this, the model fits in the noise in the data rather than the feature.

The wind direction affects the orientation of dunes dominantly found on the Martian surface as a result of prominent aeolian activity. The temporal changes of such dune landforms over large areas can be analyzed by the automatic segmentation technique. Thus, we can obtain greater insights about the wind patterns prevalent over the regions of study. For analyzing dune migration rate over a period of time, we need to detect dune and non-dune features. AI based models generated in this study has potential of automated detection of the above features and help in understanding the dune migration phenomenon. Availability of dataset was the main problem that was faced during this study. High resolution HiRISE image has less coverage as it is not covering all the dune field regions in Martian surface. Even though CTX has larger coverage as compared to HiRISE data, it is not covering all the dune fields in Martian surface. Less number of training data set also affect the model accuracy.

#### Acknowledgment

The authors acknowledge NASA PDS Geoscience Node for providing us with HiRISE and CTX data. Financial support for this work under Mars Orbiter Mission Announcement of Opportunity (MOM-AO) project from Space Application Centre, Indian Space Research Organization, Department of Space, Government of India also acknowledged.

#### References

- [1] Ameur H., Helali A., Nasri M., Maaref H., (2014), Improved feature extraction method based on Histogram of Oriented Gradients for pedestrian detection, GSCIT 2014 Global Summit on Computer and Information Technology, (June). doi: 10.1109/GSCIT.2014.6970120.
- [2] Amiri M., Brooks R., Behboodi B., Rivaz H., (2020). Two-stage ultrasound image segmentation using U-Net and test time augmentation. International Journal of Computer Assisted Radiology and surgery,

- Vol.15, No.6, p 981-988, doi:10.1007/s11548-020-02158-3
- Avenash R., and Viswanath P., (2019), Semantic segmentation of satellite images using a modified cnn with hard-swish activation function, VISIGRAPP 2019 - Proceedings of the 14th International Joint Conference on Computer Vision, Imaging and Computer Graphics Theory and Applications, 413-420. 4(Visigrapp), doi: 10.5220/0007469604130420.
- Azzaoui M. A., Masmoudi L., Belrhiti H. El and Chaouki I. E. (2019), Segmentation of Crescent Sand Dunes in High Resolution Satellite Images using a Support Vector Machine for Allometry, International Journal of Advanced Computer Science and Applications. Vol. 10, No.11, p 191-198.
- Bandeira L., Marques J.S, Saraiva J. and Pina P (2012), Advances in automated detection of sand dunes on Mars, Earth surface processes and Landforms, Vol.38, No. 3, p 275-283, 10.1002/esp.3323
- Bandeira L., J. Saraiva, P. Pina, (2007). Impact crater recognition on Mars based on a probability volume created by template matching. IEEE Trans. Geosci. Remote Sens. Vol.45. No.12, pp. 4008-4015.
- Benediktsson J. A., Pesaresi M. and Amason K., (2003), Classification and Feature Extraction for Remote Sensing Images from Urban Areas Based on Morphological Transformations. IEEE Transactions on Geoscience and Remote Sensing. Vol 41. No.9. p 1940-1949.
- Borg A., Boldt M., Rosander O and Ahlstrand J., (2020), E-mail classification with machine learning and word embeddings for improved customer support, Neural Computing and Applications, Vol. 33, p 1881-1902, https://doi.org/10.1007/s00521-020-05058-4
- Bouferdous N., Guilbert E. and Daniel S., "New Approach for Underwater Dunes Segmentation Using Deep Learning," OCEANS 2024 - Halifax, Halifax, NS, Canada, 2024, pp. 1-6, doi: 10.1109/OCEANS55160.2024.10754079.
- [10] Breed C.S., Grolier M. J. and McCauley J.F. (1979), Morphology and Distribution of Common 'Sand' Dunes on Mars: Comparison With the Earth. Journal Of Geophysical Research. Vol. 84, No. B14, p 8183-
- [11] Chao L. and Zhibao D. (2022), Distribution of Dune Landform on Mars. Front. Astron. Space Sci. Vol. 9, doi: 10.3389/fspas.2022.811702
- [12] Chen L., Papandreou G., Kokkinos I, Murphy K, Yuille A.L. (2016), DeepLab: Semantic Image Segmentation with Deep Convolutional Nets, Atrous Convolution, and Fully Connected CRFs, IEEE Transactions on Pattern Analysis and Machine Intelligence, Vol.20, No.20, p 1-14. 10.1109/TPAMI.2017.2699184.

- [13] Clancy R. T., Sandor B.J., Wolff M.J., Christensen P.R., Smith M.D., Pearl J.C., Conrath B.J., Wilson R.J. (2000), An intercomparison of ground-based millimeter, MGS TES, and Viking atmospheric temperature measurements: Seasonal and interannual variability of temperatures and dust loading in the global Mars atmosphere. Journal of Geophysical Research. Vol. 105. No. E4. p 9553-9571. doi: 10.1029/1999JE001089
- [14] Dalal N. and Triggs B., (2005), Histograms of Oriented Gradients for Human Detection. IEEE Computer Society Conference on Computer Vision and Pattern Recognition (CVPR'05), p 886-893 Vol. 1, doi: 10.1109/CVPR.2005.177.
- [15] Diakogiannis F. I., Waldner F., Caccetta P. and Wu C (2020), 'ResUNet- a: A deep learning framework for semantic segmentation of remotely sensed data, ISPRS Journal of Photogrammetry and Remote 94-114. Sensing, Vol. 162. 10.1016/j.isprsjprs.2020.01.013.
- [16] Gomez D., Salvador P., Sanz J., Casanova C. and Casanova J. L., (2018), Detecting Areas Vulnerable to Sand Encroachment Using Remote Sensing and GIS Techniques in Nouakchott, Mauritania. Remote sensing. Vol.10, No.10, doi: 10.3390/rs10101541.
- [17] Gupta D., (2023), Image Segmentation Keras: Implementation of Segnet, FCN, UNet, PSPNet and other models in Keras, Computer Vision and Pattern Recognition, https://doi.org/10.48550/arXiv.2307.13215
- [18] Ding Z., Zhao J., Wang J., Lai Z., (2020), Yardangs on Earth and implications to Mars: A review. Geomorphology, Vol. 364, doi: 10.1016/j.geomorph.2020.107230.
- [19] Edwards C. S., Nowicki K.J., Christensen P.R., Hill J., Gorelick N. and Murray K. (2011), Mosaicking of global planetary image datasets: 1. Techniques and data processing for Thermal Emission Imaging System (THEMIS) multi-spectral data, Journal of Geophysical Research, Vol.116, No. E10, p 1-21, doi: 10.1029/2010JE003755.
- [20] Fawdon P., Skok J.R., Balme M.R., Vye-Brown C.L., Rothery D.A. and Jordan C.J., (2015), The geological history of Nili Patera, Mars, Journal of Geophysical Research: Planets, Vol.120, No.5, p 951-977, doi:10.1002/2015JE004795.
- [21] Fenton L. K., Toigo A.D. and Richardson M. I. (2005), Aeolian processes in Proctor Crater on Mars: Mesoscale modeling of dune-forming winds, Journal of geophysical research: planets, Vol. 110, No. E6, p. 1-18. doi: 10.1029/2004JE002309.
- [22] Fenton L. K., and R. K Hayward, (2010), Geomorphology Southern high latitude dune fields on Mars: Morphology, aeolian inactivity, and climate change. Geomorphology, 121 pp. 98-121. doi: 10.1016/j.geomorph.2009.11.006.

- [23] Fenton L.K. Michaels T.I. and Beyer R.A., (2013), Inverse maximum gross bedform-normal transport 1: How to determine a dune-constructing wind regime using only imagery, Icarus, Vol.230, p 5–14. doi: 10.1016/j.icarus.2013.04.001.
- [24] Ghadiry M., Shalaby A. and Koch B., (2012), A new GIS-based model for automated extraction of Sand Dune encroachment case study: Dakhla Oases, western desert of Egypt, The Egyptian Journal of Remote Sensing and Space Sciences, Vol. 15, p. 53– 65. doi: 10.1016/j.ejrs.2012.04.001.
- [25] Gonzales C. and W. Sakla (2019), Sematic segmentation of Clouds in satellite Imagery using deep pre-trained U-Nets, 2019 IEEE Applied Imagery Pattern Recognition Workshop (AIPR), Washington, DC, USA, 2019, pp. 1-7, doi: 10.1109/AIPR47015.2019.9174594.
- [26] Greeley R., 1979. Silt-clay aggregates on Mars. Journal of Geophysical research. Vol. 84, p. 6248–6254.
- [27] Greeley R., Kuzmin R.O. and Haberle R.M., (2000), Aeolian process and their effects on understanding the chronology of Mars, Space Science Reviews: Vol.96, p 393-404
- [28] Guzewich S. D., Newman C.E., Juárez M.T, Wilson R.J, Lemmon M., Smith M.D., Kahanpää H. and Harri A.M., (2016), Atmospheric tides in Gale Crater, Mars, Icarus. Vol. 268, p 37–49. doi: 10.1016/j.icarus.2015.12.028.
- [29] Haykin S., 2009, Neural networks and learning Machines, Third edition
- [30] Hayward R. K., Fenton L.K. and Titus T.N. (2014). Mars Global Digital Dune Database (MGD3): Global Dune Distribution and Wind Pattern Observations. Icarus, Vol.230, p 38–46. doi: 10.1016/j.icarus.2013.04.011
- [31] He K., Zhang X., Ren S. and Sun J., (2016), Deep residual learning for image recognition, Proceedings of the IEEE Computer Society Conference on Computer Vision and Pattern Recognition, p 770–778. doi: 10.1109/CVPR.2016.90.
- [32] Hedin S. 1903, 'Central Asia and Tibet, Towards the holy city of Lassa, hurst and blackett limited, London.
- [33] Hood. D.R., Ewing R.C., Roback K.P., Runyon K., Avouac J. and McEnroe M., (2021), Inferring airflow across Martian dunes from ripple patterns and dynamics, Frontiers in earth science, Vol. 9, doi: 10.3389/feart.2021.702828
- [34] Hu J., Shen L., Albanie S., Sun G. and Wu E., (2018), Squeeze-and-Excitation Networks. IEEE/CVF Conference on Computer Vision and Pattern Recognition. p 7132-714, doi: 10.1109/CVPR.2018.00745.
- [35] Ivanovsky L., Khryashchev V., Pavlov V. and Ostrovskaya A. (2019), Building detection on aerial images using U-NET neural networks. Conference of

- Open Innovation Association, FRUCT, pp. 116–122. doi: 10.23919/FRUCT.2019.8711930.
- [36] Jha D., Smedsrud P.H., Riegler M. A, Johansen D., Lange T.D. and Halvorsen P., (2019), ResUNet++: An Advanced Architecture for Medical Image Segmentation. Proceedings - 2019 IEEE International Symposium on Multimedia, ISM 2019, p. 225–230. doi: 10.1109/ISM46123.2019.00049.
- [37] Kieffer H. H., 2013. Thermal model for analysis of Mars infrared mapping. Journal of Geophysical Research. Vol.118, pp. 451–470. doi: 10.1029/2012JE004164.
- [38] Lai C. Q., and S. S. Teoh, 2016. An efficient method of HOG feature extraction using selective histogram bin and PCA Feature reduction. Advances in Electrical and Computer Engineering, vol.16, pp. 101–108. doi: 10.4316/AECE.2016.04016.
- [39] Le H. T., and Pham H. T. Thu, (2018), Brain tumor segmentation using U-Net based fully convolutional networks and extremely randomized trees. Vietnam Journal of Science, Technology and Engineering. Vol.60. pp. 19–25. doi: 10.31276/vjste.60(3).19.
- [40] Liu N., He T., Tian Y., Wu B., Gao J. and Xu Z., (2020), Common-azimuth seismic data fault analysis using residual UNet.Interpretation. Vol. 8, No.3., p SM25–SM37. doi: 10.1190/INT-2019-0173.1.
- [41] Lorenz R., (2019), Yardangs and Dunes: Minimumand Maximum-Dissipation Aeolian Landforms, Earth System Dynamics Discussions. p. 1–13. doi: 10.5194/esd-2019-73.
- [42] Lu A, Wu Z., Jiang Z., Wang W., Hasi E. and Wang Y., (2024), DCVI<sup>2</sup>: Leveraging deep vision models to support geographers' visual interpretation in dune segmentation, AI Magazine, 45:472–485, DOI: 10.1002/aaai.12199
- [43] Lucas A. Rodriguez S., Narteau C., Charnay B., Pont S.C., Tokano T., Garcia A., Thiriet M., Hayes A.G., Lorenz R.D. and Aharonson O., (2014), Growth mechanisms and dune orientation on Titan, Geophysical research letters, Vol 41, No.17, p. 6093-6100, https://doi.org/10.1002/2014GL060971
- [44] Martin T. Z., Bridges N.T., Murphy J.R., (2003), Near-surface temperatures at proposed Mars Exploration Rover landing sites. Journal of Geophysical Research. Vol.108, No. E12, doi: 10.1029/2003je002063.
- [45] Martins R., P. Pina, J.S. Marques, M. Silveira, (2009). Crater detection by a boosting approach. IEEE Geosci. Remote Sens. Lett. Vol. 6. No.1, pp. 127–131.
- [46] Mckee E. D., (1979) 'A Study of Global Sand Seas'.
- [47] Mubarak W., Abouhaligah H. and Abuelgasim A., (2019), Monitoring the movement of sand dunes in the Nili patera caldera on mars using hirise images, Ninth International Conference on Mars 2019 (LPI Contrib. No. 2089), p. 6024, doi:10.13140/RG.2.2.11983.94885

- [48] Palafox L. F., Hamilton C.W., Scheidt S.P. and Alvarez A.M., (2017), Automated detection of geological landforms on Mars using Convolutional Neural Networks, Computers and Geosciences, 48-56. Vol.101. pp. 10.1016/j.cageo.2016.12.015.
- [49] Palucis, M.C., Dietrich W.E., Williams R. M. E., Hayes A.G., Parker T., Sumner D.Y., Mangold N., Lewis K. and Newsom H., (2016), Sequence and relative timing of large lakes in Gale crater (Mars) after the formation of Mount Sharp, Journal of Geophysical research: Planets, Vol.121. No.3. pp. 472-496. doi:10.1002/2015JE004905
- [50] Pashaei, M., Kamangir H., Starek M.J. and Tissot P., (2020). Review and Evaluation of Deep Learning Architectures for Efficient Land Cover Mapping with UAS Hyper-Spatial Imagery: A Case Study Over a Wetland. Remote sensing. Vol.12. No.959. pp. 1-29. doi: 10.3390/rs12060959.
- [51] Rampe E.B., Blake D.F., Bristow T.F., Ming D.W., Vaniman D.T., Morris R.V., Achilles C.N., Chipera S.J., Morrison S.M., Tu V.M., Yen A.S., Castle N., Downs G.W., Downs R.T., Grotzinger J.P, Hazen R.M., Treiman A.H., Peretyazhko T.S., Des Marais D.J., Walroth R.C., Craig P.I., Crisp J.A., Lafuente B., Morookian J.M., Sarrazin P.C., Thorpe M.T., Bridges J.C., Edgar L.A., Fedo C.M., Freissinet C., Gellert R., Mahaffy P.R., Newsom H.E., Johnson J.R., Kah L.C., Siebach K.L., Schieber J., Sun V.Z., Vasavada A.R., Wellington D. and Wiens R.C. (2019), Mineralogy and geochemistry of sedimentary rocks and eolian sediments in Gale crater, Mars: A review after six years of exploration with Curiosity, Geochemistry, Vol 80 No. 2. 125605. https://doi.org/10.1016/j.chemer.2020.125605
- [52] Runyon K.D. Bridges N.T., Ayoub F., Newman C.E., Quade J.J., (2016), An integrated model for dune morphology and sand fluxes on Mars, Earth and Planetary science Letters, Vol.451, pp.204-212, https://doi.org/10.1016/j.epsl.2016.09.054
- [53] Ronneberger O., Fischer P., and Brox T. (2015). U-Net: Convolutional Networks for Biomedical Image Segmentation. Medical Image Computing and Computer-Assisted Intervention - MICCAI 2015, Vol. 9351, pp.234–241. doi:10.1007/978-3-319-24574-4 28
- [54] Rubanenko L., Pérez-López S., Schull J. and. Lapôtre M. G. A, (2021) Automatic Detection and Segmentation of Barchan Dunes on Mars and Earth Using a Convolutional Neural Network, IEEE Journal of Selected Topics in Applied Earth Observations and Remote Sensing, vol. 14, pp. 9364-9371, doi: 10.1109/JSTARS.2021.3109900.
- [55] Sagan C. and R.A. Bagnold (1975), Fluid transport on Earth and aeolian transport on Mars. Icarus. vol.26. No.2, pp.209-218.
- [56] Saleh H. M., Saad N.H. and Isa N.A.M (2019). Overlapping chromosome segmentation using U-

- Net: Convolutional networks with test time augmentation. Procedia Computer Science. Vol.159, pp. 524–533. doi: 10.1016/j.procs.2019.09.207.
- [57] Sánchez-Bayton M., Tréguier E., Herraiz M. and Martin P., (2012) Structures near Olympia Undae, North Pole of Mars, European Planetary Science Congress 2012, Vol. 7 EPSC2012-749 2012.
- [58] Sánchez-Bayton M., M. Herraiz, P. Martin, B. Sánchez-Cano, E. Tréguier, A. Kereszturi (2022), Morphological analyses of small and medium size landforms in Scandia Cavi and Olympia Undae, Northern circumpolar region of mars, Planetary and Space Science, Volume 210, 105389, ISSN 0032-0633, doi: 10.1016/j.pss.2021.105389.
- [59] Sands W., and Monument N., (2007), 'GEOLOGY OF SAND DUNES', pp. 1–11.
- [60] Saood A., and Hatem I., (2021) 'COVID-19 lung CT image segmentation using deep learning methods: U-Net versus SegNet'. BMC Medical Imaging. Vol. 21(1), pp. 1–10. doi: 10.1186/s12880-020-00529-5.
- [61] Schwenzer S.P., Abramov O., Allen C.C., Bridges J.C., Clifford S.M., Filiberto J., Kring D.A, Lasue J., McGovern P.J., Newsom H.E., Treiman A.H., Vaniman D.T., Wiens R.C. and Wittmann A., (2012), Gale Crater: Formation and post-impact hydrous environments, Planetary and space science, Vol.70, pp.84-95, https://doi.org/10.1016/j.pss.2012.05.014
- [62] Schatz V., Tsoar H., Edgett K.S., Parteli E.J.R. and Herrmann H.J., (2007), Evidence for indurated sand dunes in the Martian north polar region. Journal of geophysical research. Vol.111, No. E04006. doi: 10.1029/2005JE002514.
- [63] Shumack S., Hesse P. and Farebrother W., (2020), Deep learning for dune pattern mapping with the AW3D30 global surface model. Earth Surface **Processes** and Landforms. Vol.45, No.11. doi:10.1002/esp.4888
- [64] Silburt A., M. Ali'-Dib, C. Zhu, A. Jackson, D. Valencia, Y. Kissin, D. Tamayo, K. Menou, (2019), Lunar crater identification via deep learning, Icarus, Vol.317, pp 27-38.
- [65] Singh T. P., Singh R.R., Himanshu, Mishra A. and Sharma N., (2020). Semantic Segmentation of Satellite Images: A Survey. International Research Journal of Engineering and Technology (IRJET). vol.07. No.12. pp. 390-393.
- [66] Smith B. A., 1972. V a r i a b l e Features on M a r s: Preliminary Mariner 9 Television Results. Icarus. Vol.17. 346-372. https://doi.org/10.1016/0019-1035(72)90005-X
- [67] Tsoar H., (2008), Types of Aeolian Sand Dunes and Geomorphological Formation. mechanics. pp. 403-429. doi: 10.1007/3-540-45670-
- [68] Ulmas P. and I. Liiv (2020), Segmentation of Satellite Imagery using U-Net Models for Land

- Cover Classification. IEEE Access. pp. 1–11. Available at: http://arxiv.org/abs/2003.02899.
- [69] Urbach E.R. and Stepinski T.F., (2009), Automatic detection of sub-km craters in high resolution planetary images, Planetary and Space Science, Vol.57, No. 7, doi: 10.1016/j.pss.2009.03.009
- [70] Urso A., Chojnacki M. and Vaz D.A., (2018), Dune-Yardang Interactions in Becquerel Crater, Mars. Journal of geophysical research: planets. Vol.123. No.2. pp. 353–368. doi: 10.1002/2017JE005465.
- [71] Vasavada A. R., et al. (2012). Assessment of environments for Mars Science Laboratory entry, descent, and surface operations. Space Science Reviews, Vol.170, pp 793-835, doi: 10.1007/s11214-012-9911-3.
- [72] Vasilev I., Slater D., Spacagna G., Roelants P. and Zocca V. (2019), Exploring deep learning techniques and neural network architectures with PyTorch, Keras, and TensorFlow, Python deep learning, second edition
- [73] Vaswani A., Shazeer N., Parmar N., Uszkoreit J., Jones L., Gomez A.N., Kaiser L. and Polosukhin I., (2017). Attention is all you need. 31st Conference on Neural Information Processing Systems (NIPS 2017). pp.1-15
- [74] Wagner F. H., Dalagnol R., Tarabalka Y., Segantine T.Y.F., Thome R. and Hirye M.C.M., (2020). U-Netid, an instance segmentation model for building extraction from satellite images-Case study in the Joanopolis City, Brazil. Remote Sensing, Vol.12, No.10, pp. 1–14. doi: 10.3390/rs12101544.
- [75] Wang J., Xiao L., Reiss D., Hiesinger H., Huang J., Xu Y., Zhao J., Xiao Z. and Komatsu G., (2018), Geological Features and Evolution of Yardangs in the Qaidam Basin, Tibetan Plateau (NW China): A Terrestrial Analogue for Mars. Journal of Geophysical Research: Planets, Vol.123, No.9, pp. 2336–2364. doi: 10.1029/2018JE005719.
- [76] Wang Z. T., Wang H.T., Niu Q.H, Dong Z.B. and Wang T., (2011), Abrasion of yardangs. Physical Review Vol.84, No.3, doi: 10.1103/PhysRevE.84.031304.
- [77] Wray J.J. 2013, Gale crater: the Mars Science Laboratory/Curiosity Rover Landing Site, International Journal of Astrobiology Vol.12, No.1, pp 25–38 (2013) doi:10.1017/S1473550412000328.
- [78] Wolff M.J., Bell III J.F., Malin M.C., Caplinger M.A., Fahle J., Cantor B.A., James P.B., Ghaemi T., Posiolova L.V., Ravine M.A., Supulver K.D., Calvin W.M., Clancy R.T., Edgett K.S., Edward L.J., Haberle R.M., Hale A., Lee S.W, Rice M.S., Thomas P.C. and Williams R.M.E., (2013), Calibration and Performance of the Mars Reconnaissance Orbiter Context Camera (CTX), MARS The international journal of Mars science and exploration, MARS 8, pp 1-14, 2013; doi:10.1555/mars.2013.0001
- [79] Xu K., Ba J., Kiros R., Chao K., Courville A., Salakhutdinov R., Zemel R. and Bengio Y., (2015),

- Show, attend and tell: Neural image caption generation with visual attention. 32nd International Conference on Machine Learning, ICML 2015, 3, pp. 2048–2057.
- [80] Zhang Z., Q. Liu, and Y. Wang, (2018), Road Extraction by Deep Residual U-Net.IEEE Geoscience and Remote Sensing Letters. Vol.15, No.5, pp. 749–753. doi: 10.1109/LGRS.2018.2802944
- [81] Zhao, P.; An, J.; Zheng, J., Han, W.; Tuerxun, N.; Cui, B.; Zhao, X., Segmentation Performance and Mapping of Dunes in Multi-Source Remote Sensing Images Using Deep Learning. Land 2025, 14, 713. https://doi.org/10.3390/land14040713
- [81] https://www.analyticsvidhya.com/blog/2021/05/convolutional-neural-networks-cnn/
- [82] https://www.visobyte.com/2023/04/maskrcnnunet-comparison-of-two-image-segmentationmethods.html

# **Funding**

Financial support through a project grant under an Announcement of Opportunity (AO) for Mars Orbiter Mission (Mangalyan) project from Indian Space Research Organization, Department of Space through the Scheme ISRO/SSPO/MOM-AO/2016-17 and grant no. 19013/28/2016-sec.2 is gratefully acknowledged.